

Vibration-based damage localization and quantification in a pretensioned concrete girder using stochastic subspace identification and particle swarm model updating

Structural Health Monitoring
XX(X):2–31
©The Author(s) 2018
Reprints and permission:
sagepub.co.uk/journalsPermissions.nav
DOI: 10.1177/ToBeAssigned
www.sagepub.com/


Alessandro Cancelli¹, Simon Laflamme^{1,2}, Alice Alipour¹, Sri Sritharan¹, Filippo Ubertini³

Abstract

A popular method to conduct structural health monitoring is the spatio-temporal study of vibration signatures, where vibration properties are extracted from collected vibration responses. In this paper, a novel methodology for extracting and analyzing distributed acceleration data for condition assessment of bridge girders is proposed. Three different techniques are fused enabling robust damage detection, localization and quantification. First, stochastic subspace identification is used as an output-only method to extract modal properties of the monitored structure. Then, a reduced order stiffness matrix is reconstructed from the SSID data using the system equivalent reduction expansion process. Third, a particle swarm optimization algorithm is used to update a finite element model (FEM) of the bridge girder to match the extracted reduced order stiffness matrix and modal properties. The proposed approach is first verified through numerically simulated data of the girder and then validated using experimental data obtained from a full-scale pretensioned concrete beam that experienced two distinct states of damage. Results show that the method is capable of localizing and quantifying damages along the girder with good accuracy, and that results can be used to create a high fidelity finite element model (FEM) of the girder that could be leveraged for condition prognosis and forecasting.

Keywords

Vibration-Based, Particle Swarm, Output Only

1 INTRODUCTION

2 Condition-based maintenance of transportation infrastructures is emerging as a cost-
3 effective solution to allocate limited resources to the aging infrastructure problem. Unlike
4 traditional breakdown-based and time-based strategies [1], condition-based maintenance
5 has the potential to decrease costs from the improved efficiency of maintenance and
6 repair decisions [2]. This requires knowledge of structural conditions that are typically
7 evaluated through visual inspection, which is a process known to be lengthy, costly
8 and subjective. An alternative is to automate the inspection process through structural
9 health monitoring (SHM) methods. SHM generally consists of collecting, processing
10 and interpreting a continuous set of data measured from a set of sensors installed on
11 a structure to diagnose, localize and prognose the extent of damage, and/or evaluating
12 and forecasting structural conditions based on the retrieved information. A challenge
13 in deploying SHM solutions to civil structures and structural members is in the large
14 geometries under consideration, whereas sensors need to be strategically deployed in
15 order to provide rich-enough data that can yield to condition-based information [3]. This
16 can be done using sparse [4] and dense [5] networks of sensors measuring strain [6, 7],
17 acceleration [8, 9, 10, 11], and other [12, 13, 14] states.

18 Acceleration-based SHM solutions have shown promise due to the possibility of
19 retrieving global modal information from a structure. This vibration-based method
20 generally consists of associating damage with changes in modal properties [15]. Among
21 these approaches, Operational Modal Analysis (OMA) [16] using stochastic subspace
22 identification (SSID) is of high interest due to the capability of identifying structural
23 modal properties using only the measured structural response, also termed an output-only
24 method. A notable advantage of SSID-based methods is their suitability for automated
25 implementations [17, 18, 19, 20, 21], making them a powerful tool for SHM purposes.
26 SSID can be conducted through either covariance-driven (SSID-COV) [22] or data-
27 driven (SSID-DATA) algorithms. SSID-DATA is of particular interest, because modal
28 parameters can be identified directly from the measured time signal, unlike the SSID-
29 COV where one needs to obtain the covariance matrix relating all of the measured

¹Department of Civil, Construction, and Environmental Engineering, Iowa State University, Ames, IA 50011, USA

²Department of Electrical and Computer Engineering, Iowa State University, Ames, IA 50011, USA

³Department of Civil and Environmental Engineering, University of Perugia, Perugia 06125, Italy

Corresponding author:

Alessandro Cancelli, Department of Civil, Construction, and Environmental Engineering, Iowa State University, Ames, IA 50011, USA.

Email: acancell@iastate.edu

1 system outputs. An exhaustive summary on these methods and their applications to civil
2 engineering structures can be found in [23, 24, 25, 26, 27, 28].

3 Many applications of SSID have been proposed and demonstrated. For instance,
4 Peeters *et al.* [29] proposed the combination of SSID and auto-regressive exogenous
5 (ARX) methods for damage detection applied to the Z24 Bridge benchmark case study.
6 Acceleration data from the Z24 Bridge were analyzed using SSID to obtain the evolution
7 of the first four modes as a function of wearing surface temperature. Subsequently, an
8 ARX model was used to relate temperature to frequencies and produce a predictive
9 model. The prediction error data was then used as the damage detection feature. Also
10 using the Z24 Bridge benchmark, Kullaa [30] proposed a damage detection approach
11 combining SSID and statistical control charts. SSID was used to retrieve the structural
12 modal properties under different damage conditions. The information was grouped
13 using mode pairing based on a minimal Euclidean distance criteria. The grouped modal
14 properties were then used to construct statistical control charts, whose bounds were used
15 as the damage detection feature. Outside the Z24 benchmark, Su *et al.* [31] proposed a
16 damage detection method for multi-story frame buildings based on the combination of
17 the SSID and the Gram-Schmidt orthogonalization process. Acceleration data collected
18 under earthquake excitation were analyzed through a wavelet-based SSID approach to
19 identify frequencies and mode shapes. Mode shapes were mass-normalized and corrected
20 using the Gram-Schmidt orthogonalization process, followed by the construction of a
21 diagonal modal stiffness matrix used for damage detection.

22 Similar to other OMA and vibration-based SHM methods, several sources of
23 uncertainty such as material properties, non-white noise and non-stationary loading, as
24 well as changes in environmental and operational conditions, may affect the performance
25 of the algorithm to relate changes in modal properties to damage. A solution to
26 overcome this challenge is to treat the damage identification task as an optimization
27 problem. Using this strategy, the identified modal properties are used in combination
28 with a structural model to build specific optimization functions. Optimization algorithms
29 are used to minimize the error in the dynamic properties of the model with respect
30 to the real structure, enabling accurate damage location and quantification [32, 33].
31 Popular algorithms include the metaheuristics approaches (e.g., PSO, firefly algorithms)
32 [34, 35, 36, 37, 38], hybridized metaheuristics approaches (e.g., PSO/simplex algorithm)
33 [39, 40] and stochastic/deterministic methods (e.g., Nelder-Mead methods) [34, 15]. In
34 particular, Meruane and Heylen [41] proposed a combination of SSID with a genetic
35 algorithm. The authors used SSID to retrieve the system's modal properties, which
36 were then combined with a structural model to build optimization functions. A genetic
37 algorithm was used to perform the optimization, yielding localization and quantification
38 of damage.

39 The authors of this paper have initiated work on a method that while combining SSID
40 with an optimization algorithm, integrates model reduction methods to reconstruct a
41 higher resolution finite element model (FEM) of the monitored structure. Preliminary
42 findings were published in conference proceedings [42, 43]. The method, which
43 constitutes the novelty of this paper, consists of extracting modal information, including
44 modal frequencies and shapes, using an SSID algorithm. Subsequently, a reduced

order stiffness matrix is reconstructed based on the system equivalent reduction expansion process (SEREP). At the final stage, a FEM is reconstructed and updated by optimizing three newly developed optimization functions. The approach selected for the optimization purpose in this study was a particle swarm optimization (PSO) algorithm, due to its flexibility and ease of implementation. It must be noted that other optimization strategies could have been utilized. The PSO performed the optimization of the three different functions, and this result was used to achieve damage localization and quantification. The damage detection capabilities of the framework was verified using simulation data [42], and model updating capabilities validated using experimental data [43]. Work presented here extends the previous framework by defining new, refined optimization functions and by validating the damage detection process using data collected from a laboratory test of a full-scale bridge girder. The modified algorithm is first tested using simulated data from a simply supported reinforced concrete (RC) beam. Then, the proposed method is validated using experimental data obtained on a full-scale pretensioned concrete (PC) girder subjected to white noise excitation that mimics realistic operational traffic loading.

In what follows, the theoretical background of the proposed method, including the SSID approach, the SEREP method and the PSO technique, is presented. Then, the SSID-based algorithm is introduced. Finally, the results from both the numerical simulations and full-scale laboratory tests are presented, and the paper is concluded.

Background

The proposed damage identification and quantification technique leverages the SSID, SEREP, and PSO algorithms. This section summarizes the theoretical background for each of these methods.

Stochastic subspace identification

SSID is a dynamic analysis tool that is generally used for retrieving natural frequencies, mode shapes and modal damping from output-only data. Dynamic properties are obtained through a linear state-space representation reconstructed directly from measured data. Consider the discrete-time state space representation of a linear time-invariant dynamic system [44]:

$$\begin{aligned}\mathbf{x}_{k+1} &= \mathbf{A}\mathbf{x}_k + \mathbf{w}_k \\ \mathbf{y}_k &= \mathbf{C}\mathbf{x}_k + \mathbf{v}_k\end{aligned}\tag{1}$$

where the subscript k indicates a discrete step, \mathbf{x} is the state vector, \mathbf{A} the state matrix, \mathbf{y} the output vector, \mathbf{C} the output matrix, \mathbf{w} and \mathbf{v} the zero-mean Gaussian process and excitation noise vector, respectively. Both Gaussian processes are defined by their covariance matrix Σ :

$$\Sigma = \begin{bmatrix} \mathbf{L}_k & \mathbf{SS}_{\mathbf{w},\mathbf{v}} \\ \mathbf{SS}_{\mathbf{w},\mathbf{v}}^T & \mathbf{Z}_v \end{bmatrix}\tag{2}$$

where \mathbf{L}_k is the variance matrix of \mathbf{w} , \mathbf{Z}_v the variance matrix of \mathbf{v} , and $\mathbf{SS}_{\mathbf{w},\mathbf{v}}$ is the covariance matrix between both Gaussian processes.

To conduct the SSID-DATA procedure [22] a block Hankel matrix \mathbf{H} is first constructed from the measured data. The dimension of this matrix depends on two user-defined quantities $2i$ and j , which represent the matrix's number of output row blocks and columns, respectively.

$$\mathbf{H}_i = \begin{bmatrix} y(0) & y(1) & \dots & y(j-1) \\ y(1) & y(2) & \dots & y(j) \\ \vdots & \vdots & \ddots & \vdots \\ y(i-1) & y(i) & \dots & y(i+j-2) \\ \hline y(i) & y(i+1) & \dots & y(i+j-1) \\ y(i+1) & y(i+2) & \dots & y(i+j) \\ \vdots & \vdots & \ddots & \vdots \\ y(2i-1) & y(2i) & \dots & y(2i+j-2) \end{bmatrix} = \begin{bmatrix} \mathbf{Y}_p \\ \mathbf{Y}_f \end{bmatrix} \quad (3)$$

Matrix \mathbf{H}_i is subdivided into submatrices \mathbf{Y}_p and \mathbf{Y}_f , usually termed past and future output block matrices. Both submatrices have i block rows and j columns, where $j \leq s-2i+1$ and s is the total number of time samples available. The block Hankel matrix is decomposed using the QR-factorization:

$$\mathbf{H}_i = \begin{bmatrix} \mathbf{Y}_p \\ \mathbf{Y}_f \end{bmatrix} = \mathbf{R}\mathbf{Q}^T \quad (4)$$

where \mathbf{Q} is a square orthonormal matrix of dimension j such that $\mathbf{Q}^T\mathbf{Q} = \mathbf{Q}\mathbf{Q}^T = \mathbf{I}_j$ with \mathbf{I}_j being the identity matrix of dimension j , and \mathbf{R} is a lower triangular matrix of dimension $f \times j$ with f being the total number of sensors. Using the decomposition of the Hankel matrix, the orthogonal projection \mathcal{P}_i of the past row space into the future row space is computed as:

$$\mathcal{P}_i = \mathbf{Y}_f/\mathbf{Y}_p = \mathbf{Y}_f\mathbf{Y}_p^T(\mathbf{Y}_p\mathbf{Y}_p^T)^\dagger\mathbf{Y}_p = \begin{bmatrix} \mathbf{R}_{2,1} \\ \mathbf{R}_{3,1} \\ \mathbf{R}_{4,1} \end{bmatrix} \mathbf{Q}_1^T \quad (5)$$

where $(\cdot)^\dagger$ is the Moore-Penrose pseudo-inverse, $\mathbf{R}_{2,1}$, $\mathbf{R}_{3,1}$, $\mathbf{R}_{4,1}$ are submatrices of \mathbf{R} , and \mathbf{Q}_1 is a submatrix of \mathbf{Q} . The projection is expressed as a product between the observability matrix of the system \mathbf{O}_i and a Kalman filter state sequence $\hat{\mathbf{X}}_i$:

$$\mathcal{P}_i = \begin{bmatrix} \mathbf{C} \\ \mathbf{CA} \\ \mathbf{CA}^2 \\ \vdots \\ \mathbf{CA}^{i-2} \end{bmatrix} \begin{bmatrix} \hat{\mathbf{x}}_i & \hat{\mathbf{x}}_{i+1} & \dots & \hat{\mathbf{x}}_{i+j-1} \end{bmatrix} = \mathbf{O}_i\hat{\mathbf{X}}_i \quad (6)$$

Both \mathbf{O}_i and $\hat{\mathbf{X}}_i$ are retrieved through the singular value decomposition (SVD) of the projection as follows:

$$\mathcal{P}_i = \mathbf{U}\mathbf{S}\mathbf{V}^\top \quad (7)$$

$$\mathbf{O}_i = \mathbf{U}\mathbf{S}^{1/2} \quad (8)$$

$$\hat{\mathbf{X}}_i = \mathbf{O}_i^\dagger \mathcal{P}_i \quad (9)$$

1 where \mathbf{U} , \mathbf{S} and \mathbf{V} are the matrices obtained from the SVD. An overdetermined set of
2 linear equations is obtained from the estimated Kalman filter state sequence as follows:

$$\begin{bmatrix} \hat{\mathbf{X}}_{i+1} \\ \mathbf{Y}_i \end{bmatrix} = \begin{bmatrix} \mathbf{A} \\ \mathbf{C} \end{bmatrix} \hat{\mathbf{X}}_i + \begin{pmatrix} \rho_w \\ \rho_v \end{pmatrix} \quad (10)$$

3 where \mathbf{Y}_i is a Hankel matrix with only one row block, while ρ_w and ρ_v are the residuals
4 of the modelling and data noise, respectively. Solving this overdetermined problem by a
5 least square approach yields matrices \mathbf{A} and \mathbf{C} in a discrete-time form:

$$\begin{bmatrix} \mathbf{A} \\ \mathbf{C} \end{bmatrix} = \begin{bmatrix} \hat{\mathbf{X}}_{i+1} \\ \mathbf{Y}_i \end{bmatrix} \hat{\mathbf{X}}_i^\dagger \quad (11)$$

6 The retrieved \mathbf{A} matrix can be decomposed using its eigenvalues and eigenvectors
7 yielding:

$$\mathbf{A} = \mathbf{\Psi}_d \mathbf{\Lambda}_d \mathbf{\Psi}_d^{-1} \quad (12)$$

8

$$\mathbf{\Lambda}_d = \begin{bmatrix} \lambda_{d,1} & 0 & \dots & 0 \\ 0 & \lambda_{d,2} & \dots & 0 \\ \vdots & \vdots & \ddots & \vdots \\ 0 & 0 & \dots & \lambda_{d,n} \end{bmatrix} \quad (13)$$

where $\mathbf{\Lambda}_d$ is a diagonal matrix containing the $\lambda_{d,1}, \lambda_{d,2}, \dots, \lambda_{d,n}$ discrete time complex eigenvalues and $\mathbf{\Psi}_d$ is the discrete time complex eigenvector matrix. These discrete time quantities need to be converted into continuous time quantities to obtain the dynamic parameters of the system:

$$\mathbf{A} = e^{\mathbf{A}_c \Delta t} \quad (14)$$

$$\mathbf{C}_c = \mathbf{C} \quad (15)$$

$$\lambda_c = \frac{\ln(\lambda_d)}{\Delta t} \quad (16)$$

$$\mathbf{\Lambda}_c = \mathbf{\Lambda}_d \quad (17)$$

9 where the subscript d indicates discrete-time quantities, the subscript c indicates
10 continuous time quantities, λ is a vector containing the complex eigenvalues and Δt
11 is the time step of the measured data. The circular frequencies ω_i and modal damping ξ_i

of the system can be determined using the complex conjugates eigenvalues of the matrix \mathbf{A}_c :

$$\lambda_{c,j}, \lambda_{c,j}^* = -\xi_i \omega_i \pm (j) \omega_i \sqrt{1 - \lambda_{c,j}^2} \quad (18)$$

where the superscript $*$ indicates the complex conjugate and j is the imaginary unit. Lastly, the mode shapes matrix Φ of the system can be obtained from the continuous time eigenvectors Ψ_d as:

$$\Phi = \mathbf{C}_c \Psi_d \quad (19)$$

It follows that the dynamic properties of the structural system can be derived from the retrieved discrete-time matrices \mathbf{A} and \mathbf{C} .

In the SSID theory, the order of the system n , or the dimension of the aforementioned matrices \mathbf{A} and \mathbf{C} , should be equal to twice the number of modes needed to accurately describe the structural response. However, when analyzing full-scale structures, a higher value of n is often required to account for the possible presence of weakly excited and/or closely spaced modes. This over-modelling approach has the drawback of creating spurious modes associated with the measurements noise. To overcome this problem it has become common practice in the SSID analysis to evaluate the dynamic properties of the system over a wide range of n and i values. For the purpose of automating the separation of physical modes from the spurious ones, Ubertini et al. [20] developed a three-step automated modal identification procedure. First, the complex conjugates eigenvalues are eliminated from the results. Then, specific control criteria for frequencies, damping, and mode shapes are used to eliminate modes created from the noise in the identification process and from over-modelling. Finally, the remaining modes are clustered and the structure's modal information are selected by analyzing the stability of these modes through the similarity of the parameters in the various model's orders and number of output block rows of the block Hankel matrix.

System equivalent reduction expansion process condensation method

In the proposed algorithm, the physical system is simplified into a FEM of degrees-of-freedom (DOFs) equal to the number of sensors. This yields a reduced order model for which dynamic properties can be obtained from the SSID method. SEREP [45], is utilized to maintain equivalence between the dynamic properties of the full and reduced models. This method is used for dynamic condensation and allows for the temporal comparison of dynamic properties, leading to the quantification of changes in stiffness. A specific performance matrix is created from this method in order to improve the precision of the reconstructed stiffness of the system. To derive the expression of the SEREP reduced order stiffness matrix, $\bar{\mathbf{K}}_{\text{red},S}$, consider the matrix form of the equation of motion [44]

$$\mathbf{M}\ddot{\mathbf{x}} + \mathbf{C}_d \dot{\mathbf{x}} + \mathbf{K}\mathbf{x} = \mathbf{F}(t) \quad (20)$$

where \mathbf{M} is the mass matrix, \mathbf{C}_d the damping matrix, \mathbf{K} the stiffness matrix, $\mathbf{F}(t)$ forcing matrix, \mathbf{x} the displacement vector, and the dot denotes a time derivative. Eq. (20) can be divided into terms associated with the measured DOFs, m , and the complementary

DOFs, c :

$$\begin{bmatrix} \mathbf{M}_{mm} & \mathbf{M}_{mc} \\ \mathbf{M}_{cm} & \mathbf{M}_{cc} \end{bmatrix} \begin{bmatrix} \ddot{\mathbf{x}}_m \\ \ddot{\mathbf{x}}_c \end{bmatrix} + \begin{bmatrix} \mathbf{C}_{d,mm} & \mathbf{C}_{d,mc} \\ \mathbf{C}_{d,cm} & \mathbf{C}_{d,cc} \end{bmatrix} \begin{bmatrix} \dot{\mathbf{x}}_m \\ \dot{\mathbf{x}}_c \end{bmatrix} + \begin{bmatrix} \mathbf{K}_{mm} & \mathbf{K}_{mc} \\ \mathbf{K}_{cm} & \mathbf{K}_{cc} \end{bmatrix} \begin{bmatrix} \mathbf{x}_m \\ \mathbf{x}_c \end{bmatrix} = \begin{bmatrix} \mathbf{F}_m(t) \\ \mathbf{F}_c(t) \end{bmatrix} \quad (21)$$

To correlate the above equations with the retrieved dynamic properties of the system, a coordinate change is introduced:

$$\mathbf{x}(t) = \begin{bmatrix} \mathbf{x}_m(t) \\ \mathbf{x}_c(t) \end{bmatrix} = \Phi \mathbf{q}(t) = \begin{bmatrix} \Phi_m \\ \Phi_c \end{bmatrix} \mathbf{q}(t) \quad (22)$$

where \mathbf{x} and \mathbf{q} are associated with the physical and modal coordinates of the system, respectively, Φ_m is a matrix containing the eigenvectors of the measured DOFs, and Φ_c a matrix containing the eigenvectors of the complementary DOFs. If Φ_m is known, it is possible to derive an expression from Eq. (22) representing the modal coordinates using a least square estimator:

$$\mathbf{q} = \Phi_m^\dagger \mathbf{x}_m \quad (23)$$

Substituting Eq. (23) into Eq. (22) yields the transformation matrix for the SEREP approach:

$$\mathbf{x} = \Phi \Phi_m^\dagger \mathbf{x}_m = \mathbf{T}_r \mathbf{x}_m \quad (24)$$

$$\mathbf{T}_r = \Phi \Phi_m^\dagger \quad (25)$$

Using Eq. (24) in Eq. (20) and pre-multiplying by \mathbf{T}_r^\top leads to:

$$\mathbf{T}_r^\top \mathbf{M} \mathbf{T}_r \ddot{\mathbf{x}}_m + \mathbf{T}_r^\top \mathbf{C}_d \mathbf{T}_r \dot{\mathbf{x}}_m + \mathbf{T}_r^\top \mathbf{K} \mathbf{T}_r \mathbf{x}_m = \mathbf{T}_r^\top \mathbf{F}(t) \quad (26)$$

Expanding the term of the equation relative to the stiffness matrix and noting that $\Phi^\top \mathbf{K} \Phi = \Omega^2$ (were Φ is mass-normalized), one obtains an expression for $\bar{\mathbf{K}}_{\text{red},S}$:

$$\bar{\mathbf{K}}_{\text{red},S} = \mathbf{T}_r^\top \mathbf{K} \mathbf{T}_r = (\Phi_m^\dagger)^\top \Phi^\top \mathbf{K} \Phi \Phi_m^\dagger = (\Phi_m^\dagger)^\top \Omega^2 \Phi_m^\dagger \quad (27)$$

This condensation method preserves the selected eigenvalues of the original system through the transformation, implying that the selected mode's eigenvalues are equal for both systems. This property is independent of the location and the number of sensors. The accuracy of this approach was extensively studied by Sairajan and Aglietti [46] for complex systems, where the SEREP reduction process showed good performance, even when realistic noise was considered in the retrieved mode shapes. Also, it was demonstrated that using fewer mode shapes than the available number of sensors yielded a model that better represented the response of the original system.

Particle swarm optimization algorithm

The PSO is a probabilistic search algorithm used for optimization problems. It is based on a simplified social model derived from the behavior of animal swarms such as birds [47] and bees [48]. Using this approach, variables are optimized within a set of possible solutions termed particles. These particles are moved around the search space with a given velocity, yielding updated positions. Each particle's movement is influenced by promising locations found by other particles. The process is iterated until an optimal solution is obtained. In this paper, the PSO is used to optimize the stiffness values of a simplified structural model to obtain a match between the model and the retrieved data. This is achieved by creating an initial set of particles location \mathbf{z}_1 , with random values assigned to each of them representing the values of stiffness of the elements. This set is stored in a matrix with a dimension defined by the number of variables of the problem multiplied by the swarm size. A corresponding set of random initial velocities $\dot{\mathbf{z}}_1$ for the particles is also generated. The function is evaluated for each row of the swarm matrix, and the results are used to evaluate both the swarm's best position and each single particle's best location b . The global position is taken as the row that provides the lower value for the optimization function. The local minima starts equal to the initial values assigned to each particle. When successive steps are evaluated, the local minima is defined as the step for which the optimization function is minimized for that particle. For each particle, a new velocity is calculated using a unitary time step and the gained knowledge on the best location through the following expression:

$$\dot{z}_{h+1}^r = w\dot{z}_h^r + e_1\delta_1(b^r - z_h^r) + e_2\delta_2(b_h^g - z_h^r) \quad (28)$$

where δ_1 and δ_2 are random numbers between 0 and 1, b_r is the best location found for the r^{th} particle, b_h^g the best global location at step h , w is the inertia of the particles, and e_1 , e_2 are trust parameters. The inertia regulates the action of the swarm, with larger and smaller values yielding a global and local behavior, respectively. The trust parameters represent the confidence of a particle in itself, e_1 , and in the whole swarm, e_2 . The position of each particle is updated using their previous location and the previously calculated updated velocity:

$$z_{h+1}^r = z_h^r + \dot{z}_{h+1}^r \Delta t \quad (29)$$

where z_{h+1}^r is the new location of the r^{th} particle, and Δt is a unitary value. This updating scheme is repeated until the difference between two consecutive step values of the optimization function is less than a predefined tolerance.

DAMAGE DETECTION ALGORITHM

The proposed damage detection, location, and quantification method is divided into two sequential stages. First, acceleration data is analyzed using the SSID technique to extract the natural frequencies and mode shapes of the monitored system. This information is used to create the reduced order stiffness matrices of the system along with SEREP, after normalizing the mode shapes with respect to their 2-norm. Second, the retrieved modal properties and reduced order stiffness matrices are combined with the respective

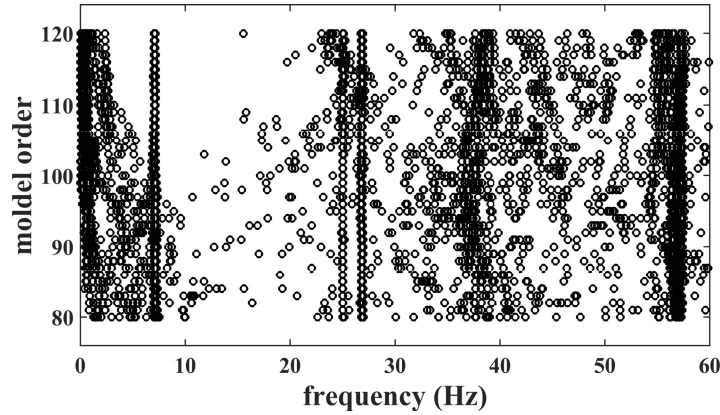


Figure 1. Retrieved frequencies versus model order n identified by the SSID algorithm before the elimination of noisy modes.

quantities calculated from the FEM to generate three optimization functions. These are processed using the PSO in an optimization process, obtaining specific damage indices used to detect, localize, and quantify damage.

Stage I - Extraction of modal properties

In Stage I, the system's frequencies \mathbf{f}_{retr} and mode shapes Φ_{retr} are extracted using the SSID technique. This is achieved through the three-step method proposed by Ubertini et al. [20] discussed above. Figure 1 shows typical raw data obtained from an SSID analysis using laboratory data from this work (to be described later), while Figure 2 shows the same data after filtering out the noisy modes. One can observe that after filtering, the first frequency of the system becomes immediately identifiable as the only stable frequency in the 0-10 Hz range. Clustering was used to identify the higher modes. The technique consists of aggregating the remaining modes into clusters that meet predefined criteria. The structural modes can be selected by analyzing the mode shapes of the clustered sets. Figure 3 shows an example of the clustering process results for the stable modes of the system (Figure 3), showing the 90% confidence interval for the damping (vertical lines) and the frequencies (horizontal lines). The first three identified modes of the system are encircled in the figure, where one intermediary mode (around 38 Hz) was not considered because it was associated with high damping. The retrieved mode shapes are normalized with respect to their 2-norm $\|\cdot\|$:

$$\Phi_{\text{retr},i} = \frac{\Phi_{\text{retr},i}}{\|\Phi_{\text{retr},i}\|} \quad (30)$$

where $\Phi_{\text{retr},i}$ is the i^{th} mode shape. The retrieved frequencies and normalized mode shapes are used to calculate the data-driven reduced order stiffness matrix $\bar{\mathbf{K}}_{\text{red},S,\text{data}}$ (Eq. (27)). The procedure to conduct Stage I is presented in Algorithm 1

Algorithm 1 Damage detection algorithm - Stage I

```

1:  $accdata \leftarrow$  input of the acceleration data
2:  $i \leftarrow Nrows_{min} \div Nrows_{max}$  ▷ Block rows range
3:  $j \leftarrow Ncol_{min} \div Ncol_{max}$  ▷ Columns Range
4:  $\epsilon_n, \epsilon_f, \epsilon_\Phi, \epsilon_\nu$  ▷ Noise and clustering parameters
5: for  $i \leftarrow Nrows_{min}, Nrows_{max}$  do
6:   for  $j \leftarrow Ncol_{min}, Ncol_{max}$  do
7:     Perform SSID for current  $i$  and  $j$ 
8:      $Raw_{data} \leftarrow SSID$  results
9:   end for
10: end for
11:  $Filtered_{data} \leftarrow Raw_{data} \geq \epsilon_n$ 
12:  $N_{freq} \leftarrow$  length of  $Filtered_{data}$ 
13: for  $f \leftarrow 1, N_{freq}$  do
14:   Frequency check  $\epsilon_f$ 
15:   Mode shape check  $\epsilon_\Phi$ 
16:   Damping check  $\epsilon_\nu$ 
17:   if Frequency check & Mode shape check & Damping check are true then
18:      $Clustered_{data} \leftarrow$  Current data
19:   end if
20: end for

```

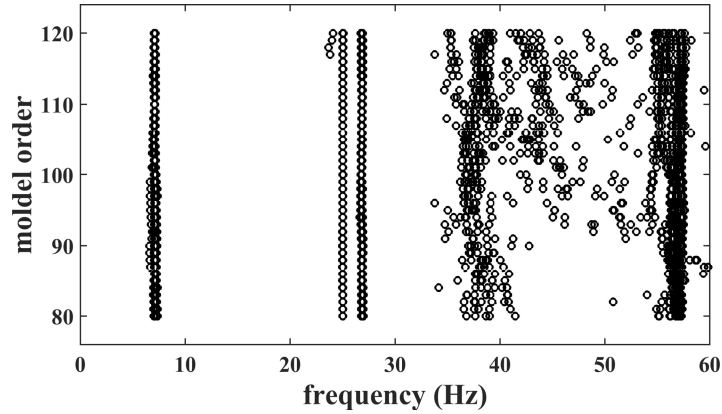


Figure 2. Retrieved frequencies versus model order n identified by the SSID algorithm after the elimination of noisy modes.

1 Stage II - Damage detection and location

2 In Stage II, a finite element model (FEM) of the structure is constructed containing
3 parameters that can be altered as a function of damage indices, α_i . These indices multiply
4 the bending stiffness EI of the model's elements, where E is the Young's modulus of
5 the material and I is the sections' moment of inertia. Note that EI can differ between

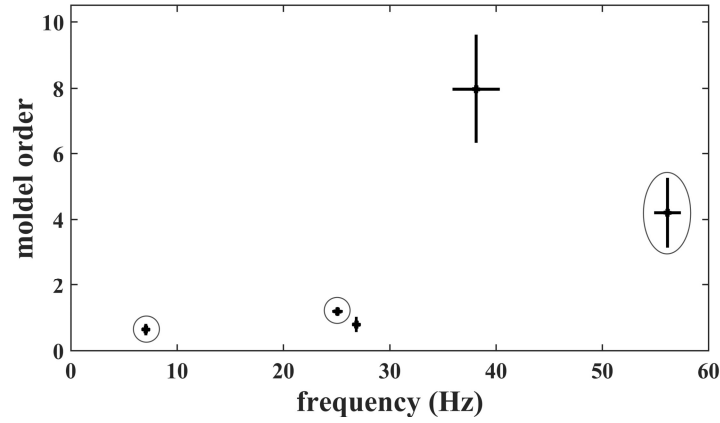


Figure 3. Retrieved frequencies versus damping ratios after the clustering process, showing the identified system modes encircled in red.

elements. Parameters α_i are selected based on an optimization function, which yield an updated FEM from which the model-driven dynamic parameters and reduced order matrices can be obtained. The described process is based on the assumption that the mass matrix of the system is known. However, this assumption can be relaxed by accounting for mass variability by introducing a second set of coefficients β_i . This set will multiply the linear mass ρA_g of each model's element, where A_g is the cross section area of the element and ρ is the material density. The remaining part of the process follows the same steps as the case for known mass, described in what follows.

Three different optimization functions are used to select parameters α_i , each solved independently, producing three different sets of damage indices. These optimization functions, termed OF_1 to OF_3 , are defined as follows.

- Optimization function OF_1 : the mean absolute percentage error between the retrieved frequencies and the frequencies obtained from the model.

$$OF_1 = \frac{1}{n_d} \sum_{d=1}^{n_d} \left(\frac{(f_{\text{retr},d} - f_{\text{funct},d})}{f_{\text{funct},d}} 100 \right) \quad (31)$$

where n_d is the number of selected frequencies, $f_{\text{retr},d}$ is the d^{th} retrieved frequency, and $f_{\text{funct},d}$ is the d^{th} frequency obtained from the model.

- Optimization function OF_2 : the mean value of the standard deviation for the ratio of the computed and retrieved mode shapes.

$$OF_2 = \frac{1}{n_d} \sum_{d=1}^{n_d} \left(\frac{1}{n_s - 1} \sum_{s=1}^{n_s} (\Phi_{ds,rt} - \bar{\Phi}_{d,rt})^2 \right) \quad (32)$$

$$\Phi_{ds,rt} = \frac{\Phi_{\text{func},ds}}{\Phi_{\text{retr},ds}} \quad (33)$$

$$\bar{\Phi}_{d,rt} = \frac{1}{n_s} \sum_{s=1}^{n_s} \left(\frac{\Phi_{\text{func},ds}}{\Phi_{\text{retr},ds}} \right) \quad (34)$$

1 where n_s is the number of sensors, $\Phi_{\text{func},ds}$ is the s^{th} component of the d^{th} mode shape
2 function and $\Phi_{\text{retr},ds}$ is the s^{th} component of the d^{th} retrieved mode shape.

- Optimization function OF_3 : the mean of the absolute value of all the terms in the SEREP error matrix. This matrix is defined as the absolute percentage error between the elements of the retrieved and the model's SEREP reduced order stiffness matrices.

$$OF_3 = \frac{1}{n_s} \sum_{s=1}^{n_s} \left(\frac{1}{n_s} \sum_{z=1}^{n_s} (k_{S,\text{diff},sz}) \right) \quad (35)$$

$$k_{S,\text{diff},sz} = \left| \frac{\bar{k}_{\text{red},S,\text{data},sz} - \bar{k}_{\text{red},S,\text{func},sz}}{\bar{k}_{\text{red},S,\text{data},sz}} 100 \right| \quad (36)$$

3 where $\bar{k}_{\text{red},S,\text{data},sz}$ and $\bar{k}_{\text{red},S,\text{func},sz}$ are the elements in position sz of the retrieved and
4 model's SEREP reduced order stiffness matrices, respectively.

5 These functions are solved using the PSO algorithm. Damage detection, location, and
6 quantification is conducted by comparing all three sets of α_i selected by the particle
7 optimization swarm. To detect damage, all of the three α_i for a given element must to
8 be below unity, where unity is associated with the undamaged condition. If all α_i are
9 different than unity for a given element, then damage is considered to be associated with
10 that element, identifying the damage location. This criteria was established to minimize
11 the identification of false positives. The quantified level of damage corresponds to the
12 average value of α_i for that particular element. For example, an average value of $\alpha_i = 0.6$
13 would signify an element at 60% of its original health, or 40% damaged. Algorithm 2
14 details the implementation procedure of the damage detection approach.

15 NUMERICAL VERIFICATION AND LABORATORY VALIDATION

16 In this section, the proposed algorithm is first verified through numerical simulations
17 on a reinforced concrete girder. Then, it is validated using a laboratory experiment on a
18 pretensioned concrete girder.

19 Numerical verification

20 The simulated system consists of a simply supported reinforced concrete beam of 13.0
21 m (42.65 ft) length. The beam, illustrated in Figure 4, is discretized into 16 elements of

Algorithm 2 Damage detection algorithm - Stage II

```

1: Clustereddata  $\leftarrow$  Import from Stage I
2:  $OF_1 \leftarrow Eq.(31)$ 
3:  $OF_2 \leftarrow Eq.(32)$ 
4:  $OF_3 \leftarrow Eq.(35)$ 
5:  $Swarmsize, N_{variables}$   $\triangleright$  Number of particles and problem variables
6:  $toll \leftarrow 10^{-4}$   $\triangleright$  Stopping criteria value
7: Initializing damage indices
8: for  $j \leftarrow 1, 3$  do
9:    $\alpha_{i, OF_j} \leftarrow \Re^{Swarmsize \times N_{variables}}$ 
10: end for
11: Parallel evaluation of the functions
12: for  $j \leftarrow 1, 3$  do
13:    $OF_{j,1} = OF_j(\alpha_{i, OF_j})$ 
14:    $k \leftarrow 2$ 
15:   while  $OF_{j,k} - OF_{j,k-1} \geq toll$  do
16:      $b_k^g \leftarrow \min(OF_{j,k})$ 
17:      $b^r \leftarrow \min(OF_{j,k}(r), OF_{j,k-1}(r))$   $\triangleright r = 1 \div Swarmsize$ 
18:      $k = k + 1$ 
19: Parallel evaluation of the functions optimization
20:   for  $r \leftarrow 1, Swarmsize$  do
21:      $\dot{z}(k+1)^r \leftarrow Eq.(28)$ 
22:      $z(k+1)^r \leftarrow Eq.(29)$ 
23:   end for
24: end while
25:    $\alpha_{OF_j} \leftarrow \min(OF_{j,k}(r))$ 
26: end for
27: for  $r \leftarrow 1, N_{variables}$  do
28:   if  $\alpha_{OF_1}(r) \& \alpha_{OF_2}(r) \& \alpha_{OF_3}(r) < 1$  then
29:      $\alpha(r) \leftarrow \text{mean}(\alpha_{OF_1}(r), \alpha_{OF_2}(r), \alpha_{OF_3}(r))$ 
30:   else
31:      $\alpha(r) \leftarrow 1$ 
32:   end if
33: end for

```

1 equal length and a rectangular cross-section of $0.3 \times 0.6 \text{ m}^2$ ($11.8 \times 23.6 \text{ in}^2$). Two
2 different damage scenarios are simulated to assess the performance of the proposed
3 approach. In the first scenario, damage is introduced in the system by reducing the
4 moment of inertia for elements 7 and 8 by 20 and 30%, respectively, to represent the
5 effects of crack formation in a neighboring region. In the second scenario, damage is
6 introduced by reducing the moment of inertia for elements 9 and 13 by 30 and 20%,
7 respectively, to represent damage at two distinct locations. The beam is excited using a

Table 1. First three frequencies of the system, retrieved with SSID and calculated from the model before damage

mode	model frequency (Hz)	SSID frequency (Hz)	error (%)
1	5.730	5.743	-0.22
2	22.920	22.867	0.23
3	51.567	51.501	0.13

dynamic moving load that mimics the passage of a vehicle (shown by $f(t)$, Figure 4) for a total duration of 60 s. This type of excitation was selected to test the robustness of the algorithm over non-ideal conditions. When the excitation is not white noise, its frequency will appear in the retrieved modal properties. However, using the method proposed by Ubertini et al. [20], it is possible to overcome this problem by automatically eliminating this spurious pole. Such result is quite relevant to field applications, where the excitation cannot always be characterized as white noise. Gaussian white noise was added to the excitation force to simulate the ambient vibrations. This noise was characterized using the signal-to-noise (SNR) ratio, expressed in dB:

$$\text{SNR} = 20 \log_{10} \left(\frac{A_{\text{signal}}}{A_{\text{noise}}} \right) \quad (37)$$

where A_{signal} is the root mean square of the noisy signal (i.e., the excitation force), and A_{noise} is the root mean square of the noise. For this study, the SNR was set to 70 dB. The application of white noise in the excitation force generated an SNR of 11.25 dB or 37.7% noise in the collected response data. The apparent high amplification of the noise level from the excitation to the response is due to the fact that both the exciting force and the white noise generate a comparable level of acceleration in the system. Figure 5 plots the acceleration response from the force (i.e., noise-free) and from the noise itself. These responses have comparable magnitude generating a high level of SNR in the final response. In this study, a low magnitude force was selected in order to produce a high level of noise for assessing the robustness of the SSID identification process.

Rayleigh damping was used in the simulation, assigning to the first two modes a damping ratio of 3%. The corresponding structural response was taken at three locations simulating three sensors (locations s_1 , s_2 , and s_3 in Figure 4). Figure 4 shows plots of a typical excitation and a corresponding numerically measured acceleration time series.

Results from the modal properties extraction process using SSID for the first three modes before damage are listed in Table 1. There is excellent agreement between the modes from the model and those extracted using SSID.

For each scenario, the modal properties retrieved after damage are used to construct the three optimization functions (OF_i) along with a surrogate beam model. In each PSO analysis, the values of the damage indices α_i were allowed to vary between 0.4 and 1.0. The PSO for these functions yielded three sets of damage indices for each scenario, α_i , listed in Table 2. For the first scenario, results showed that only elements

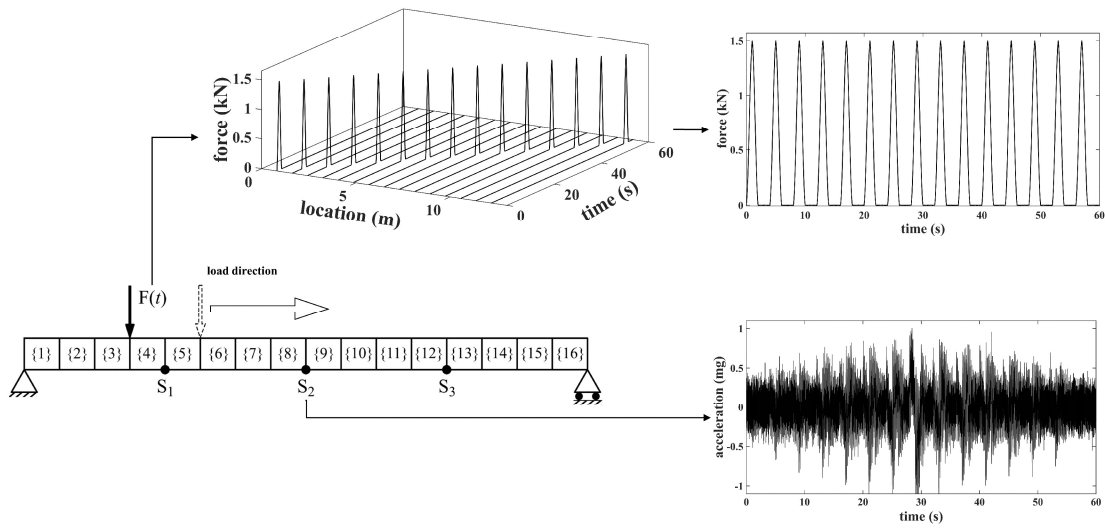


Figure 4. Simulated simply supported RC girder showing element discretization, sensors locations (s_1 , s_2 , and s_3), and example of force input and acceleration response time series.

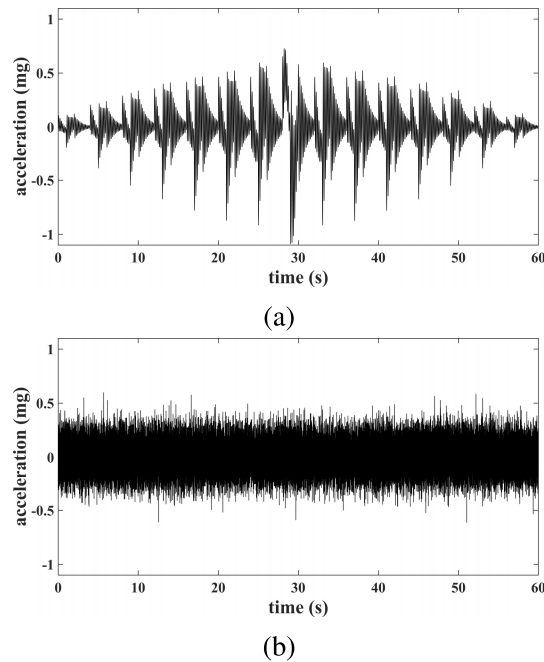


Figure 5. Responses of the system from the noise-free (a) and noise-only (b) simulations.

7 and 8 passed the rejection criteria, since all their damage indices α_i were smaller

Table 2. Damage indices α_i obtained from the particle swarm analysis for the three optimization functions

element number	first damage scenario				second damage scenario			
	OF_1	OF_2	OF_3	final	OF_1	OF_2	OF_3	final
	α_i	α_i	α_i	α_i	α_i	α_i	α_i	α_i
1	1.00	0.40	0.93	1.00	1.00	0.40	1.00	1.00
2	1.00	0.70	0.99	1.00	1.00	1.00	1.00	1.00
3	1.00	1.00	1.00	1.00	1.00	1.00	0.83	1.00
4	1.00	0.95	1.00	1.00	1.00	1.00	1.00	1.00
5	1.00	0.97	0.98	1.00	1.00	1.00	1.00	1.00
6	1.00	0.94	0.52	1.00	1.00	1.00	1.00	1.00
7	0.81	0.95	0.68	0.81	1.00	0.78	1.00	1.00
8	0.70	0.67	0.81	0.73	1.00	1.00	1.00	1.00
9	0.88	1.00	0.85	1.00	0.73	0.75	0.69	0.72
10	1.00	0.77	0.84	1.00	1.00	1.00	1.00	1.00
11	1.00	0.91	0.92	1.00	1.00	0.78	1.00	1.00
12	0.95	1.00	0.96	1.00	1.00	0.94	1.00	1.00
13	0.90	1.00	1.00	1.00	0.68	0.88	0.80	0.79
14	1.00	0.52	0.98	1.00	1.00	1.00	1.00	1.00
15	1.00	0.96	0.98	1.00	1.00	1.00	1.00	1.00
16	1.00	1.00	0.97	1.00	1.00	1.00	1.00	1.00

1 than unity for all three optimization functions. The average α_i values for elements
 2 7 and 8 were $\alpha_7 = 0.81$ and $\alpha_8 = 0.73$, respectively, which correspond to identified
 3 damages of 19% and 27% comparable with the simulated damages of 20% and 30%, for
 4 element 7 and 8, respectively. Similarly, in the second damage scenario, results indicate
 5 presence of damage only at elements 9 and 13. The average damage indices returned a
 6 value of $\alpha_9 = 0.72$ and $\alpha_{13} = 0.79$ for elements 9 and 13, respectively, yielding and
 7 identified damage intensity of 28% and 21% that compares well with the simulated
 8 damage of 30% and 20%, respectively. Under both damage cases, the algorithm correctly
 9 identified the damage location and its intensity. However, the PSO algorithm includes
 10 random generations (Eq. (28)) that could affect the results. To evaluate the effect of such
 11 randomness, the second damage scenario was analyzed using five different runs. In each
 12 run, the random number generator used in the Matlab environment was changed in type
 13 and seed. The results of this analysis, in terms of the final average indices, are shown
 14 in Figure 6. All of the five runs detected and diagnosed damage under elements 9 and
 15 13 only. The average value of the damage indices between all the runs was equal to
 16 $\alpha_9 = 0.72$ and $\alpha_{13} = 0.80$ for elements 9 and 13, respectively, with a standard deviation
 17 of $\sigma_{\alpha_9} = 0.02$ and $\sigma_{\alpha_{13}} = 0.01$, respectively. These results indicates that the PSO's
 18 random generation feature has limited effect on the localization and identification of the
 19 damage intensity.

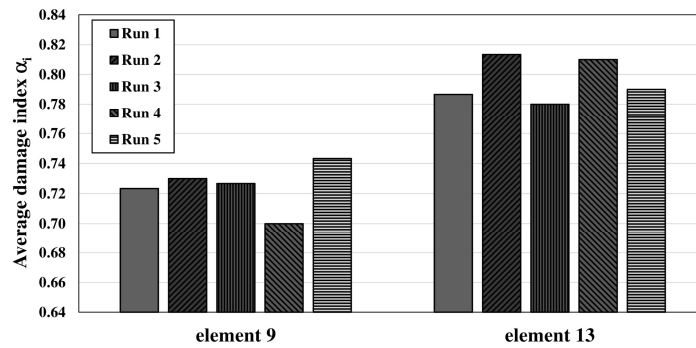


Figure 6. Variation of the average damage index α_i between different runs for the elements 9 and 13.

1 Laboratory validation

2 The laboratory validation is conducted on a full-scale pretensioned girder built with a
 3 partial cast-in-place deck, identified as BTC60. BTC60 was a standard pre-stressed bulb-
 4 tee type C girder designed by the Iowa Department of Transportation with a span of 18.3
 5 m (60 ft), part of a larger set of experiments conducted under NCHRP project 12-94. The
 6 girder had a depth of 1.14 m (45 in) and its partial deck is extended symmetrically about
 7 the mid-span over a total length of 6.8 m (22.3 ft). Flexural cracking on the girder was
 8 expected outside the partial deck region. Figure 7 shows the cross-sectional dimensions
 9 of both the girder (Figure 7(a)) and composite (Figure 7(b)) sections. The girder was built
 10 using a 41.36 MPa (6 ksi) concrete with eight 1.52 mm (0.6 in) low relaxation strands,
 11 applying a total initial prestressing force of 1514 kN (340.3 kips). The deck was cast in
 12 place using a specified concrete strength of 27.60 MPa (4 ksi). The concrete strengths on
 13 the day of testing were 51.17 MPa (7.422 ksi) and 33.15 MPa (4.808 ksi) for the girder
 14 and deck, respectively.

15 To acquire dynamic response measurements, BTC60 was excited using an RMK-
 16 2200 servo hydraulic shaker, controlled through the LabVIEW environment, applying
 17 a white noise excitation over 80 s with an amplitude of ± 4.45 kN (1 kip) and
 18 standard deviation of 0.89 kN (0.20 kip), which generated response accelerations
 19 ranging between 50-150 mg. The shaker was offset by 1.52 m to the side of the
 20 girder's center line, which corresponded with the possible installation position closest
 21 to the center line due to the presence of loading equipment. Four 16 mm bolts for
 22 concrete were used to secure the shaker to the girder. Figure 8 and Figure 9 show
 23 the shaker location in the experimental setup. For safety, chains were used to loosely
 24 connect the beam ends to the supports (Figure 8). The response of the structure was
 25 collected using nine accelerometers mounted to the bottom surface of the girder, and
 26 one accelerometer installed on the actuator masses. Two different types of Seismic ICP
 27 uniaxial piezoelectric accelerometers were used for this experiment: five model 393C,
 28 and four model 393B04 from PCB. Data was acquired through LabVIEW environment

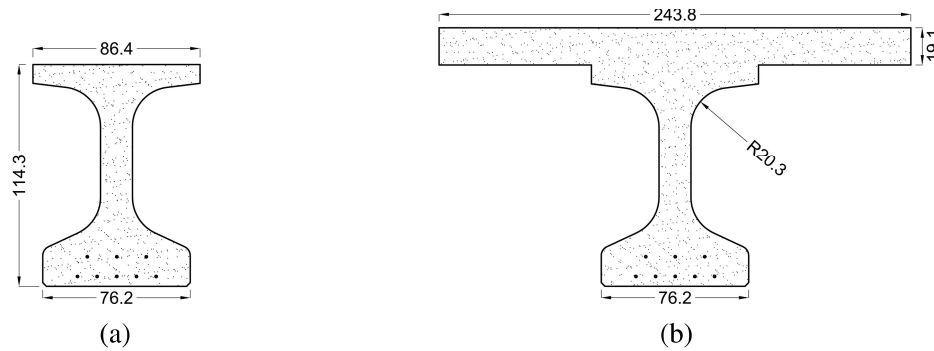


Figure 7. BTC60: schematic of (a) girder; and (b) composite cross sections (all dimensions in centimeters).

using four NI9234 modules with a sampling rate of 1652 Hz. Figure 8 shows the location of the shaker and sensors whereas Figure 9 illustrates the experimental setup.

Three different damage cases were considered. Damage was induced in the girder using a pair of actuators mounted onto the top of the beam (Figure 8). These damage stage are characterized by the intensity of the load applied to the girder, summarized as follows:

- *No damage:* The girder was subjected to a monotonic quasi static load with maximum intensity of 44.5 kN (10 kips). Upon reaching this value, the beam was fully unloaded and a dynamic shaking test was performed. This first loading step ensured that the system was behaving as expected in the undamaged elastic region. This first test was aimed at acquiring measurements for the undamaged condition of the structure, representing the stiffness of the undamaged specimen.
- *Damage case 1:* The next step in the loading protocol of the beam consisted of reaching 80% of the predicted yield load of the girder-deck system, corresponding to 355.9 kN (80 kips). Under this load the girder experienced a deflection of 2.54 cm (1 in). During this phase, the formation and growth of 10 to 13 flexural cracks, in the portion of the girder within the partial deck, was confirmed by visual inspection. Following the visual confirmation of damage, the beam was unloaded and subjected to the dynamic shaking test.
- *Damage Case 2:* The final damage stage represents the condition where the strands in the extreme location of the girder have reached the first yield limit state, which occurred at 452.4 kN (101.7 kips). A mid-span deflection of 8.1 cm (3.19 in) was recorded. Due to the high load both the extension of the previously formed cracks and the formation of new ones were observed. After unloading the beam, a final set of dynamic tests was conducted.

No damage case

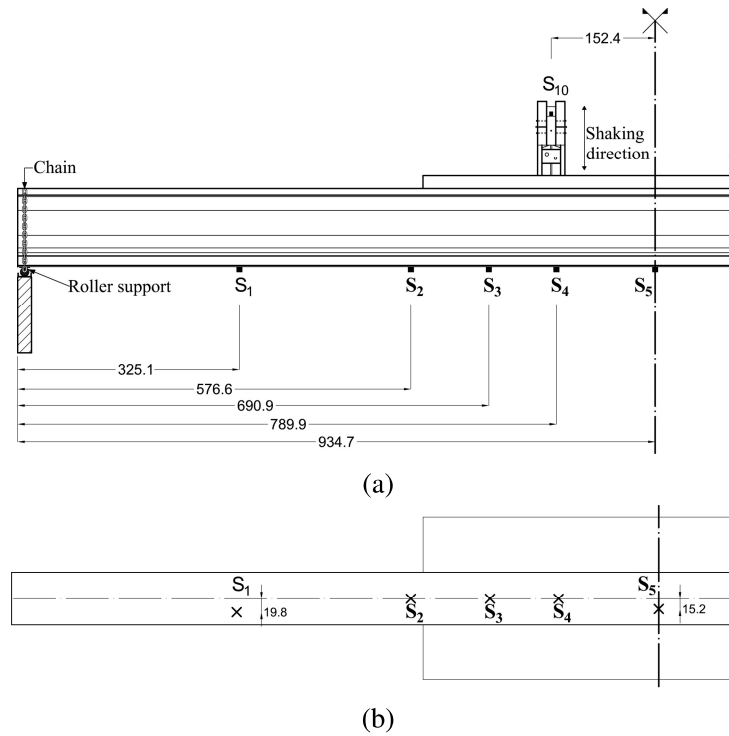


Figure 8. Sensors and shaker locations (a) side view and (a) bottom view (all dimensions in centimeters, sensors s_6 to s_9 are placed symmetrically with respect to the mid-span).

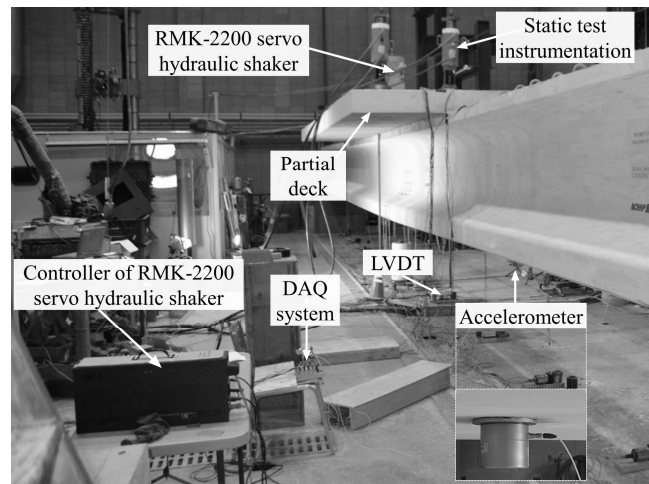


Figure 9. Experimental setup of BTC60 with seismic ICP uniaxial piezoelectric accelerometers model and the hydraulic shaker.

- 1 The tested beam was modeled in MATLAB as a two-dimensional structure,
- 2 discretizing the beam into 36 elements of variable lengths (shown in Figure 10). The
- 3 beam was first divided based on sensor locations, and then a small element of length
- 4 0.1778 m (7 in) was defined to account for the offset of the deck with respect to sensors

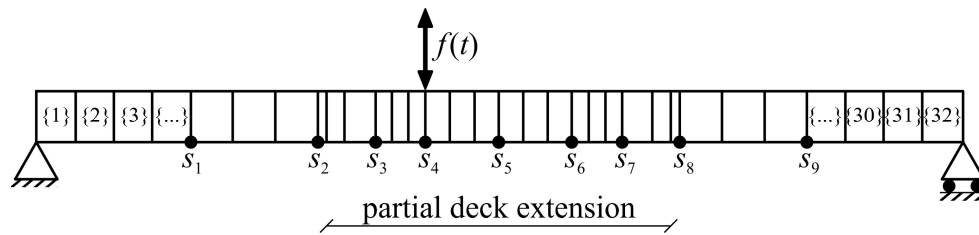


Figure 10. Finite element model (FEM) discretization for the BTC60.

Table 3. First three frequencies of the system retrieved with the SSID compared with the ones from the NUM and the UM

mode	SSID frequencies (Hz)	NUM frequencies (Hz)	NUM error (%)	UM frequencies (Hz)	UM error (%)
1	7.06	6.92	1.96	7.04	0.28
2	25.09	25.91	-3.30	24.98	0.40
3	56.15	58.59	-4.30	57.17	-1.82

s_2 and s_8 . The remaining portions of the model were divided into smaller elements, with length ranging from 0.3302 m (13 in) to 0.8382 m (33 in), to achieve a more accurate representation of the girder dynamics. Figure 10 schematizes the discretized model, in which $f(t)$ indicates the force from the shaker. The properties of the MATLAB model are estimated from the specimen's construction plans. This preliminary model is termed the non-updated model (NUM).

The model was then updated using the measured structural responses. Measured data were first filtered using a Chebyshev Type II low-pass filter to eliminate high frequency components of noise in the data, and then analyzed using the SSID algorithm to retrieve the dynamic properties of the specimen. Unlike for the numerical simulation, the retrieved modal properties differed significantly from the NUM. This is attributed to the differences between the beam's as-designed and as-constructed. Thus, the NUM is updated to obtain the best match between the model and data. This is done by allowing the modification of the stiffness and mass terms of the elements by a factor ranging arbitrarily from 0.8 to 1.2. The damage indices, α_i , were modified to include the variation in the stiffness and mass for each element, resulting in new indices denoted by β_i and γ_i representing the change in stiffness constants and masses, respectively. The optimization functions (i.e., Eqs. (31, 32, 35)) were then solved using the PSO, yielding a new model termed updated model (UM). Table 3 compares the frequencies obtained from the SSID algorithm with those obtained from the NUM and the UM. A comparison of the errors shows that the UM resulted in a significant improvement in the modal parameters, reducing the maximum error on the frequencies from 4.30% to 1.82%. Figure 11 visually represent the modification factors for each element stiffness and mass, respectively.

The resulting model was further validated by comparing the static displacement measurements acquired from string potentiometers during the application of the static

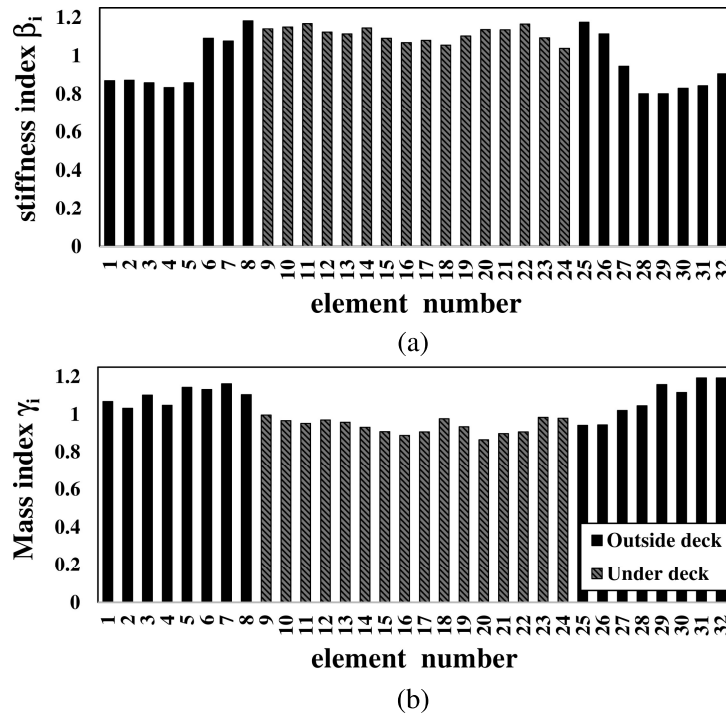


Figure 11. Modification factors (a) β_i for element stiffness and (b) γ_i for element mass.

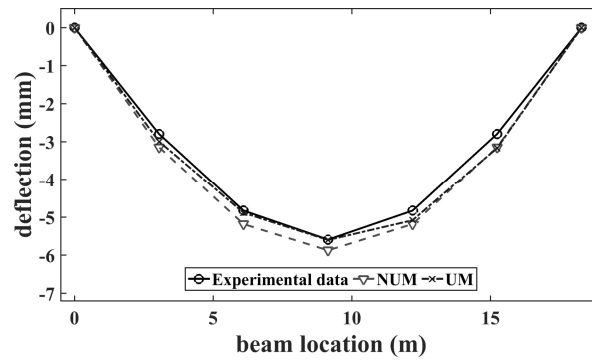


Figure 12. Comparison of the static deflection shapes.

load of 178 kN (40 kips) applied at the center of the beam. Figure 12 compares the static displacement obtained from the NUM, the UM, and experimental data. Results show better agreement between the UM and the experimental data, with a deflection error at mid-span reducing from 5.1% to 0.2%. However, fitting errors persist on the right-hand-side with no significant reduction after updating. This residual error may be attributed to an unmodeled variability in the boundary conditions, for instance from the chain used to secure the beam, and to the limited and localized excitation produced by the shaker that was located on the left-hand-side of the beam.

Table 4. Changes in frequencies due to damage case 1

mode	no damage frequencies (Hz)	damage 1 frequencies (Hz)	frequency change (%)
1	7.09	7.00	-1.27
2	25.03	24.97	-0.23
3	57.15	53.49	-6.40

Table 5. Changes in frequencies due to damage case 2

mode	damage 1 frequencies (Hz)	damage 2 frequencies (Hz)	frequency change (%)
1	7.00	6.78	-3.14
2	24.97	24.65	-1.28
3	53.49	51.27	-4.15

Damage case 1

The same data processing methodology was applied to damage case 1. The first three frequencies of the specimen are compared with the no damage case in Table 4. It can be observed that all the frequencies decreased following the introduction of damage, with the third frequency being the most sensitive.

Here, the UM is used as the reference model, and is updated to localize and quantify damage. However, only the element stiffness is modified, as it is assumed that mass remained constant. To ensure robustness of the procedure, five different runs were performed using different random number generators for the optimization process. Figure 13(a) shows the average damage indices obtained from this process while Figure 13(b) plots the standard deviation of the indices. Their values represent the fraction of bending rigidity (EI) for each element relative to the reference model. Results show that only the elements under the deck area were damaged and that the identified damage area remains consistent between different runs by yielding a zero variance at the elements outside this area. This was consistent with the observations during the experiments, as shown in Figure 14 where cracks were visually observable. This updated model is termed updated model - damage 1 (UMD1).

Damage case 2

Similar to damage case 1, Table 5 lists and compares the first three frequencies retrieved through SSID. In this case, both the first and third frequencies show higher sensitivity to damage.

For this stage, the UMD1 becomes the reference model for the damage detection process. This implies that the damage indices represent a further reduction in the

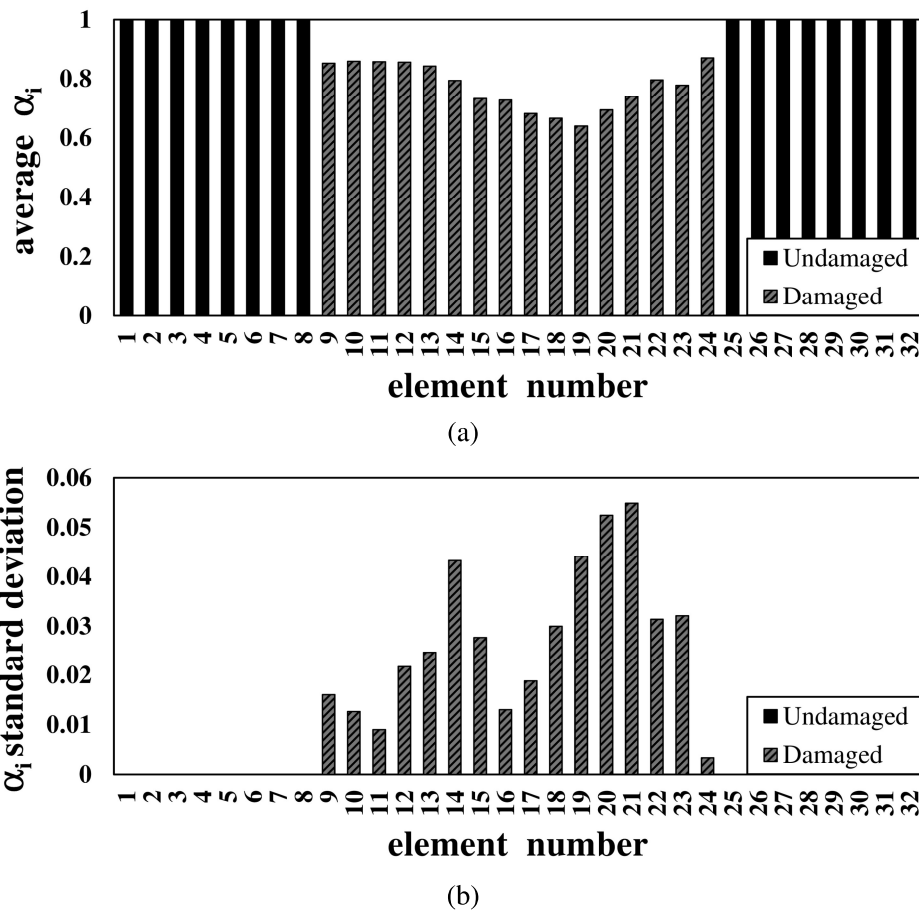


Figure 13. Damage indices for damage case 1: (a) average values and (b) standard deviations from the five runs

elements' bending rigidity from the previous analysis. Figure 15(a) illustrates the retrieved damage indices, while Figure 15(b) plots the total average damage indices that are relative to the UM. Results shows that some deterioration starts to appear outside of the deck area, but that the majority of the damage is still concentrated under the deck area. This is supported by visual observations during the test. Figure 16 is a picture of the crack pattern under damage case 2. Consistently with the previous case, the standard deviations (Figure 17) show that the damaged elements are always correctly identified through the analyzes. Also, it can be observed that the standard deviation of the damaged elements is lower than for the previous damage case. This can be attributed to the higher level of damage that is easier to identify. This further updated model is termed updated model - damage 2 (UMD2).

Lastly, the tangent stiffness is used to further validate the model. The tangent stiffness from the model is obtained by applying a unitary force at midspan and dividing the value by the midspan deflection x_{mid} . The experimental reloading stiffness was taken as the tangent of the reloading curve, obtained from the data collected using a linear variable

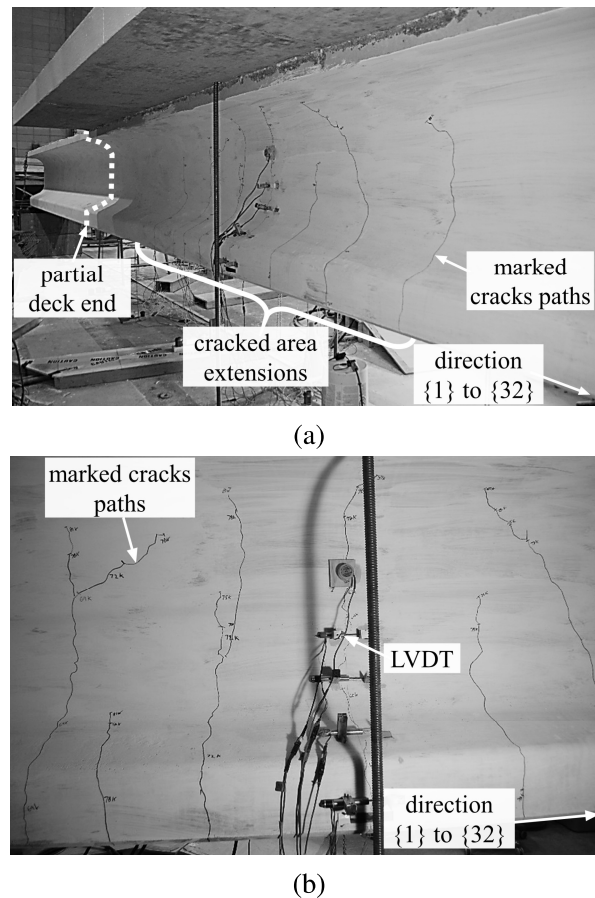


Figure 14. Crack pattern on BTC60 specimen under damage 1 condition: (a) side view and (b) detail of cracked area.

differential transformer (LVDT). The resulting model tangent stiffness is 24,826 kN/m (142 kips/in), while the experimental tangent stiffness is 25,227 kN/m (144 kip/in), a difference of 1.19 %, demonstrating a good match between the UMD2 and experimental data. This result shows that the quantification of damages from the algorithm was likely accurate. Note that due to a malfunction of the LVDT, the experimental secant stiffness could not be computed under damage case 1.

CONCLUSIONS

This paper presented a novel technique for damage detection, localization and quantification from vibration data. The method consists of 1) retrieving modal properties through an SSID algorithm; 2) reconstructing a reduced order stiffness matrix through the SEREP technique; and 3) reconstructing an FEM optimized with a PSO. By identifying the localization and quantities of altered mass and stiffness values necessary to update the FEM, the PSO was directly used for damage localization and quantification.

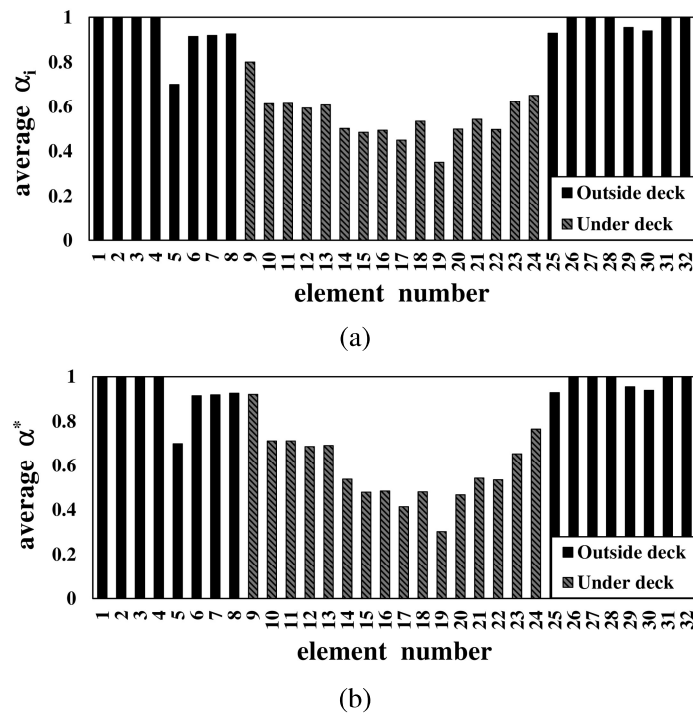


Figure 15. Damage indices for damage case 2 relative to (a) UMD1 and (b) UM.

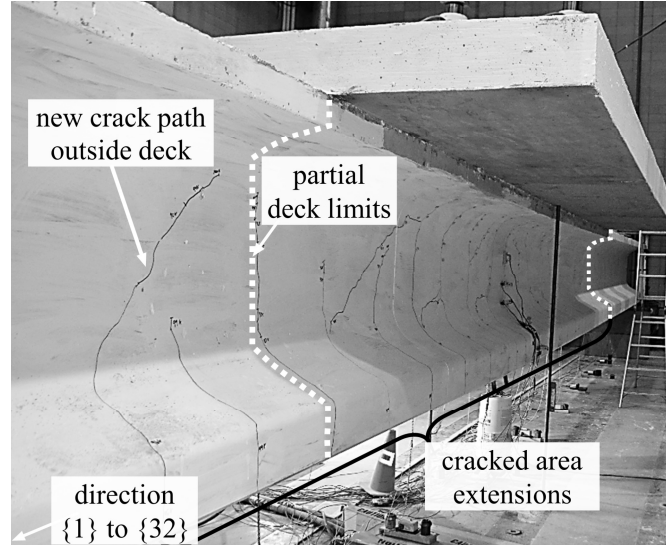


Figure 16. Crack pattern on BTC60 specimen under damage case 2.

- 1 The proposed approach was first verified on the numerical simulation of a simply
- 2 supported reinforced concrete beam. Results showed that the algorithm was capable
- 3 of detecting, localizing and quantifying damage with good accuracy under different
- 4 scenarios. After, the methodology was validated on data collected from a full-scale bridge

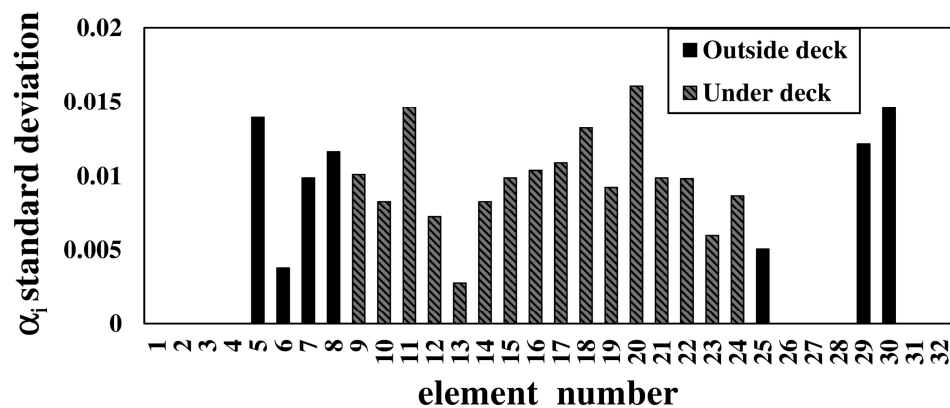


Figure 17. Standard deviation of the damage indices between the five different runs.

girder. The experiment utilized a pretensioned concrete girder excited with a white noise load using an hydraulic shaker, under the following three different damage scenarios: 1) undamaged; 2) damage case 1, pre-yielding; and damage case 2, post-yielding. Results from the undamaged specimen showed that it is possible to reconstruct a model that accurately reproduced the modal properties of the structure. Results from the damage cases demonstrated the capability of the algorithm to accurately update the FEM to identify the location of damages, supported by the visual observation of crack locations during the test. The first damage case illustrated the ability to detect damage in a confined area of the girder. On the other hand, the second damage case illustrated the capability of the algorithm to detect non-adjacent damage along the beam. While the performance of the algorithm at quantifying damage was difficult to assess, the comparison of reloading tangent stiffness values for damage case 2 showed a good match, thereby indicating that the quantification of damage was likely accurate.

It follows that the algorithm demonstrated promise at producing an accurate FEM of the monitored structure using output-only data. Such model could be used to conduct numerical analyzes furthering the assessment of the structural condition. Said information would be beneficial for condition-based maintenance procedures.

Acknowledgements

This study is partly supported by grant #65A0586 from California Department of Transportation, and grant #1537626 from the National Science Foundation. Any opinions, finding, and conclusion or recommendation expressed in this material are those of the authors and do not necessarily reflects the view of the sponsors.

References

- [1] Miwa T, Kaihara T and Nonaka Y. Integrated maintenance system trend and a maintenance scheduling system application. In *Through-life Engineering Services*. Springer International Publishing, 2014. pp. 241–268. DOI:10.1007/978-3-319-12111-6_15. URL https://doi.org/10.1007/978-3-319-12111-6_15.

- [2] Liu C, Gong Y, Laflamme S et al. Bridge damage detection using spatiotemporal patterns extracted from dense sensor network. Measurement Science and Technology 2016; 28(1): 014011. DOI:10.1088/1361-6501/28/1/014011. URL <https://doi.org/10.1088/1361-6501/28/1/014011>.
- [3] Chinde V, Cao L, Vaidya U et al. Damage detection on mesosurfaces using distributed sensor network and spectral diffusion maps. Measurement Science and Technology 2016; 27(4): 045110. DOI:10.1088/0957-0233/27/4/045110. URL <https://doi.org/10.1088/0957-0233/27/4/045110>.
- [4] Farrar C, Baker W, Bell T et al. Dynamic characterization and damage detection in the i-40 bridge over the rio grande. Technical report, 1994. DOI:10.2172/10158042. URL <https://doi.org/10.2172/10158042>.
- [5] Downey A, Ubertini F and Laflamme S. Algorithm for damage detection in wind turbine blades using a hybrid dense sensor network with feature level data fusion. Journal of Wind Engineering and Industrial Aerodynamics 2017; 168: 288–296. DOI:10.1016/j.jweia.2017.06.016. URL <https://doi.org/10.1016/j.jweia.2017.06.016>.
- [6] Ubertini F, Materazzi AL, D'Alessandro A et al. Natural frequencies identification of a reinforced concrete beam using carbon nanotube cement-based sensors. Engineering Structures 2014; 60: 265–275. DOI:10.1016/j.engstruct.2013.12.036. URL <https://doi.org/10.1016/j.engstruct.2013.12.036>.
- [7] Wipf TJ, Phares BM, Greimann LF et al. Evaluation of steel bridges (volume i): monitoring the structural condition of fracture-critical bridges using fiber optic technology. Technical report, (No. IHRB Project TR-493), 2007. URL https://lib.dr.iastate.edu/intrans_reports/209.
- [8] Kim JT and Stubbs N. Nondestructive crack detection algorithm for full-scale bridges. Journal of Structural Engineering 2003; 129(10): 1358–1366. DOI:10.1061/(asce)0733-9445(2003)129:10(1358). URL [https://doi.org/10.1061/\(asce\)0733-9445\(2003\)129:10\(1358\)](https://doi.org/10.1061/(asce)0733-9445(2003)129:10(1358)).
- [9] Liu C, DeWolf JT and Kim JH. Development of a baseline for structural health monitoring for a curved post-tensioned concrete box-girder bridge. Engineering Structures 2009; 31(12): 3107–3115. DOI:10.1016/j.engstruct.2009.08.022. URL <https://doi.org/10.1016/j.engstruct.2009.08.022>.
- [10] Doebling SW, Hemez FM, Peterson LD et al. Improved damage location accuracy using strain energy-based mode selection criteria. AIAA Journal 1997; 35(4): 693–699. DOI: 10.2514/2.159. URL <https://doi.org/10.2514/2.159>.
- [11] Ubertini F, Comanducci G and Cavalagli N. Vibration-based structural health monitoring of a historic bell-tower using output-only measurements and multivariate statistical analysis. Structural Health Monitoring: An International Journal 2016; 15(4): 438–457. DOI:10.1177/1475921716643948. URL <https://doi.org/10.1177/1475921716643948>.
- [12] Kim JT and Stubbs N. Improved Damage Identification Method Based on Modal Information. Journal of Sound and Vibration 2002; 252(2): 223–238. DOI:10.1006/jsvi.2001.3749. URL <https://doi.org/10.1006/jsvi.2001.3749>.
- [13] Yan A and Golinval JC. Structural damage localization by combining flexibility and stiffness methods. Engineering Structures 2005; 27(12): 1752–1761. DOI:10.1016/j.engstruct.2005.

- 04.017. URL <https://doi.org/10.1016/j.engstruct.2005.04.017>.
- [14] Alipour A, et al. Post-Extreme Event Damage Assessment and Response for Highway Bridges. Transportation Research Board, 2016. DOI:10.17226/24647. URL <https://doi.org/10.17226/24647>.
- [15] Nhamage IA, Lopez RH and Miguel LFF. An improved hybrid optimization algorithm for vibration based-damage detection. Advances in Engineering Software 2016; 93: 47–64. DOI:10.1016/j.advengsoft.2015.12.003. URL <https://doi.org/10.1016/j.advengsoft.2015.12.003>.
- [16] Reynders E. System identification methods for (operational) modal analysis: Review and comparison. Archives of Computational Methods in Engineering 2012; 19(1): 51–124. DOI:10.1007/s11831-012-9069-x. URL <https://doi.org/10.1007/s11831-012-9069-x>.
- [17] Rainieri C and Fabbrocino G. Automated output-only dynamic identification of civil engineering structures. Mechanical Systems and Signal Processing 2010; 24(3): 678–695. DOI:10.1016/j.ymssp.2009.10.003. URL <https://doi.org/10.1016/j.ymssp.2009.10.003>.
- [18] Andersen P, Brincker R, Goursat M et al. Automated modal parameter estimation for operational modal analysis of large systems. In Proceedings of the 2nd international operational modal analysis conference, volume 1. pp. 299–308.
- [19] Magalhães F, Cunha Á and Caetano E. Online automatic identification of the modal parameters of a long span arch bridge. Mechanical Systems and Signal Processing 2009; 23(2): 316–329. DOI:10.1016/j.ymssp.2008.05.003. URL <https://doi.org/10.1016/j.ymssp.2008.05.003>.
- [20] Ubertini F, Gentile C and Materazzi AL. Automated modal identification in operational conditions and its application to bridges. Engineering Structures 2013; 46: 264–278. DOI:10.1016/j.engstruct.2012.07.031. URL <https://doi.org/10.1016/j.engstruct.2012.07.031>.
- [21] Neu E, Janser F, Khatibi AA et al. Fully automated operational modal analysis using multi-stage clustering. Mechanical Systems and Signal Processing 2017; 84: 308–323. DOI:10.1016/j.ymssp.2016.07.031. URL <https://doi.org/10.1016/j.ymssp.2016.07.031>.
- [22] Peeters B. System identification and damage detection in civil engineering. PhD Thesis, Katholieke Universiteit te Leuven, 2000.
- [23] Peeters B, De Roeck G, Pollet T et al. Stochastic subspace techniques applied to parameter identification of civil engineering structures. In New Advances in Modal Synthesis of Large Structure.
- [24] Peeters B and Roeck GD. Reference-Based Stochastic Subspace Identification for Output-Only Modal Analysis. Mechanical Systems and Signal Processing 1999; 13(6): 855–878. DOI:10.1006/mssp.1999.1249. URL <https://doi.org/10.1006/mssp.1999.1249>.
- [25] Reynders E and Roeck GD. Reference-based combined deterministic–stochastic subspace identification for experimental and operational modal analysis. Mechanical Systems and Signal Processing 2008; 22(3): 617–637. DOI:10.1016/j.ymssp.2007.09.004. URL <https://doi.org/10.1016/j.ymssp.2007.09.004>.

- [//doi.org/10.1016/j.ymssp.2007.09.004](https://doi.org/10.1016/j.ymssp.2007.09.004).
- [26] Mevel L, Gourdat M and Basseville M. Stochastic Subspace-Based Structural Identification and Damage Detection and Localisation—Application to the Z24 Bridge Benchmark. Mechanical Systems and Signal Processing 2003; 17(1): 143–151. DOI:10.1006/mssp.2002.1552. URL <https://doi.org/10.1006/mssp.2002.1552>.
- [27] Bodeux JB and Golinval JC. Modal Identification and Damage Detection Using the Data-Driven Stochastic Subspace and ARMAV Methods. Mechanical Systems and Signal Processing 2003; 17(1): 83–89. DOI:10.1006/mssp.2002.1543. URL <https://doi.org/10.1006/mssp.2002.1543>.
- [28] Altunışık AC, Okur FY and Kahya V. Modal parameter identification and vibration based damage detection of a multiple cracked cantilever beam. Engineering Failure Analysis 2017; 79: 154–170. DOI:10.1016/j.engfailanal.2017.04.026. URL <https://doi.org/10.1016/j.engfailanal.2017.04.026>.
- [29] Peeters B, Maeck J and Roeck GD. Vibration-based damage detection in civil engineering: excitation sources and temperature effects. Smart Materials and Structures 2001; 10(3): 518–527. DOI:10.1088/0964-1726/10/3/314. URL <https://doi.org/10.1088/0964-1726/10/3/314>.
- [30] Kullaa J. Damage Detection of the Z24 Bridge Using Control Charts. Mechanical Systems and Signal Processing 2003; 17(1): 163–170. DOI:10.1006/mssp.2002.1555. URL <https://doi.org/10.1006/mssp.2002.1555>.
- [31] Su WC, Huang CS, Lien HC et al. Identifying the stiffness parameters of a structure using a subspace approach and the gram–schmidt process in a wavelet domain. Advances in Mechanical Engineering 2017; 9(7): 168781401770764. DOI:10.1177/1687814017707649. URL <https://doi.org/10.1177/1687814017707649>.
- [32] Gomes H and Silva N. Some comparisons for damage detection on structures using genetic algorithms and modal sensitivity method. Applied Mathematical Modelling 2008; 32(11): 2216–2232. DOI:10.1016/j.apm.2007.07.002. URL <https://doi.org/10.1016/j.apm.2007.07.002>.
- [33] Wei Z, Liu J and Lu Z. Structural damage detection using improved particle swarm optimization. Inverse Problems in Science and Engineering 2017; 26(6): 792–810. DOI: 10.1080/17415977.2017.1347168. URL <https://doi.org/10.1080/17415977.2017.1347168>.
- [34] Miguel LFF, Lopez RH and Miguel LFF. A hybrid approach for damage detection of structures under operational conditions. Journal of Sound and Vibration 2013; 332(18): 4241 – 4260. DOI:<https://doi.org/10.1016/j.jsv.2013.03.017>. URL <http://www.sciencedirect.com/science/article/pii/S0022460X13002496>.
- [35] Moradi S, Razi P and Fatahi L. On the application of bees algorithm to the problem of crack detection of beam-type structures. Computers and Structures 2011; 89(23): 2169 – 2175. DOI:<https://doi.org/10.1016/j.compstruc.2011.08.020>. URL <http://www.sciencedirect.com/science/article/pii/S0045794911002434>.
- [36] Kang F, Jie Li J and Xu Q. Damage detection based on improved particle swarm optimization using vibration data. Applied Soft Computing 2012; 12(8): 2329–2335. DOI:10.1016/j.asoc.2012.03.050. URL <https://doi.org/10.1016/j.asoc.2012.03.050>.

- [37] Escobar CM, González-Estrada OA and Acevedo HGS. Damage detection in a unidimensional truss using the firefly optimization algorithm and finite elements. *arXiv preprint arXiv:170604449* 2017; .
- [38] Yang XS. Firefly algorithm, lévy flights and global optimization. In *Research and Development in Intelligent Systems XXVI*. Springer London, 2009. pp. 209–218. DOI:10.1007/978-1-84882-983-1_15. URL https://doi.org/10.1007/978-1-84882-983-1_15.
- [39] Begambre O and Laier J. A hybrid particle swarm optimization – simplex algorithm (PSOS) for structural damage identification. *Advances in Engineering Software* 2009; 40(9): 883–891. DOI:10.1016/j.advengsoft.2009.01.004. URL <https://doi.org/10.1016/j.advengsoft.2009.01.004>.
- [40] Baghmisheh MV, Peimani M, Sadeghi MH et al. A hybrid particle swarm-Nelder-Mead optimization method for crack detection in cantilever beams. *Applied Soft Computing* 2012; 12(8): 2217 – 2226. DOI:<https://doi.org/10.1016/j.asoc.2012.03.030>. URL <http://www.sciencedirect.com/science/article/pii/S1568494612001287>.
- [41] Meruane V and Heylen W. Damage detection with parallel genetic algorithms and operational modes. *Structural Health Monitoring: An International Journal* 2010; 9(6): 481–496. DOI:10.1177/1475921710365400. URL <https://doi.org/10.1177/1475921710365400>.
- [42] Cancelli A, Micheli L, Alipour A et al. Identifying the extent and location of damage in a reinforced concrete girder using health monitoring data. In *Structures Congress 2017*. American Society of Civil Engineers. DOI:10.1061/9780784480427.043. URL <https://doi.org/10.1061/9780784480427.043>.
- [43] Cancelli A, Micheli L, Laflamme S et al. Damage location and quantification of a pretensioned concrete beam using stochastic subspace identification. In Wu HF, Gyekenyesi AL, Shull PJ et al. (eds.) *Nondestructive Characterization and Monitoring of Advanced Materials, Aerospace, and Civil Infrastructure 2017*. SPIE. DOI:10.1117/12.2261825. URL <https://doi.org/10.1117/12.2261825>.
- [44] Connor J and Laflamme S. *Structural Motion Engineering*. Springer, 2014. ISBN 3319062808.
- [45] Rad SZ. *Methods for updating numerical models in structural dynamics*. PhD Thesis, Department of Mechanical Engineering, Imperial College, 1997.
- [46] Sairajan KK and Aglietti GS. Robustness of system equivalent reduction expansion process on spacecraft structure model validation. *AIAA Journal* 2012; 50(11): 2376–2388. DOI: 10.2514/1.j051476. URL <https://doi.org/10.2514/1.j051476>.
- [47] Kennedy J and Eberhart R. Particle swarm optimization. In *Proceedings of ICNN'95 - International Conference on Neural Networks*, volume 4. IEEE, pp. 1942–1948. DOI:10.1109/icnn.1995.488968. URL <https://doi.org/10.1109/icnn.1995.488968>.
- [48] Venter G and Sobieszczanski-Sobieski J. Particle swarm optimization. *AIAA Journal* 2003; 41(8): 1583–1589. DOI:10.2514/2.2111. URL <https://doi.org/10.2514/2.2111>.